IEICE TRANSACTIONS

on Communications

DOI:10.23919/transcom.2024EBP3051

This advance publication article will be replaced by the finalized version after proofreading.

A PUBLICATION OF THE COMMUNICATIONS SOCIETY

The Institute of Electronics, Information and Communication Engineers

Kikai-Shinko-Kaikan Bldg., 5-8, Shibakoen 3chome, Minato-ku, TOKYO, 105-0011 JAPAN

PAPER Special Section on LaTeX 2ε Class File for the IEICE Transactions

Modeling and Statistical Characterization Analysis of Wideband Non-Stationary Channel for UAV Swarm Communication

Yunhang LIN[†], **Xiaoyu DANG**[†,††*], **Dan FEI**[†††], **Mengyao SUN**[†], **Chaoyi WANG**[†], ***Nonmembers***, ***and*** **Yongkai LIU**[†], ***Member***

SUMMARY With the rapid development of unmanned aerial vehicle (UAV) technology, UAV systems have evolved from single machine to multi-machine cooperation. Among the core technologies of UAV swarm systems, UAV swarm communication technology is increasingly receiving attention. The current modeling of UAV channels only considers communication between receiving and transmitting nodes, typically overlooking the objective situation where non-communication nodes in UAV swarm communication may interfere with the channel between two communicating nodes as they pass through.Therefore, to address this complex scenario,this paper proposes a three-dimensional wideband non-stationary channel model based on binary spheres and cylinders of heterogeneous scattering sources, incorporating line-of-sight, single-bounce, and double-bounce reflections. In this model, parameters such as the speed of the UAV swarm, distances between UAVs, departure, and arrival angles are treated as time-varying. Furthermore, statistical characteristics of the channel such as time-varying spatial-temporal-frequency correlation function and time-varying Doppler power spectral density are derived. This model not only takes into account the impact of the mobility parameters of transmitting nodes on the channel but also analyzes the influence of the motion states of non-communication nodes within the swarm on the communication channel. The simulation results demonstrate that the statistical characteristics of the wideband channel model for UAV swarms are generally similar to existing models. However, the influence of non-communication nodes on statistical characteristics cannot be ignored, with the maximum change in correlation coefficient reaching 0.29. This model provides a new practical approach for modeling UAV swarm communication channels, which can be utilized for performance evaluation and validation of UAV swarm communication systems.

key words: *Unmanned Aerial Vehicle(UAV) Swarm, multiple-input-multiple-output, channel model, statistical characteristic analysis*

1. Introduction

In recent years, the development of unmanned aerial vehicles (UAVs) technology has been rapid, playing a significant role in emergency rescue and environmental monitoring [1-2]. However, faced with an increasingly complex communication environment, UAVs have certain limitations in practical applications due to the shortcomings of their own software and hardware. As a result, UAV systems are evolving from single-machine systems to multi-machine systems [3-4]. Compared to single machines, multi-machine systems possess advantages such as autonomous control and collaborative operations [5-6], enabling them to perform more challenging tasks. Therefore, it is essential to evaluate the communication channels of UAV swarms and establish accurate and user-friendly channel models.

Currently, there has been significant progress in the field of unmanned aerial vehicle (UAV) channel measurement and modeling [7-11].Based on existing research, UAV channel models can be classified into deterministic models and stochastic models [10]. Deterministic models describe specific scenarios with high precision when based on a large amount of measured data but lack generalizability. Stochastic models include non-geometrical stochastic models (NGSM) and geometrical-based stochastic models (GBSM). Compared to NGSM, GBSM requires less measured data and provides a better reference for UAV channel modeling in data-scarce situations [11].A 3D cylindrical GBSM model was proposed in [12], while [13] presented a single-sphere-based GBSM model and derived its corresponding simulation model. However, these models do not consider the distribution of scatterers on one side of the UAV. Moreover, [14] considered a dense urban environment and proposed a dual-sphere model for unmanned aerial vehicle air-to-air (A2A) multiple-input multiple-output (MIMO) channels, accounting for scatterers at both the transmitter and receiver sides. Additionally, [15] introduced a three-dimensional elliptical cylinder UAV MIMO channel model for air-to-ground scenarios, taking into account the far-end environment of UAV communication. However, this model is a narrowband model that does not address multipath time-delay issues. Li et al. [16] proposed UAV MIMO channel models based on cylindrical and elliptical cylinders, studying the impact of UAV flight parameters such as speed and direction on channel statistical characteristics. However, the aforementioned models do not take into account the non-stationary characteristics of communication channels in UAV swarms. Through UAV channel measurements, it is evident that one of the most prominent features of UAV communication channels is their non-stationarity [17-19]. In [20], a single concentric cylinder model was employed to propose a non-stationary communication model for UAVs, utilizing the rapid movement of ground users to describe the non-stationarity of wireless channels. In [21], the use of a three-dimensional Markov mobility model was introduced to characterize UAV motion patterns. Based on this, a three-dimensional non-stationary geometric stochastic model for

[†]The authors are with the College of Electronic and Information Engineering, Nanjing University of Aeronautics and Astronautics, Nanjing, 211100, China

[††]The authors are with the Space Information Research Institute, Hangzhou Dianzi University, Hangzhou, 31018, China

[†††]The authors are with the School of Electronic and Information Engineering, Beijing Jiaotong University, Beijing, 100044, China

[*]E-mail: dang@hdu.edu.cn

air-to-air UAV communication was derived, where the mobility model can adjust the degree of randomness in movement and cover various UAV trajectories. In [22], a time-varying channel model for UAV-to-ground communication scenarios was proposed based on an aviation-based UAV trajectory model. This model simulated the non-stationarity of the channel caused by the time-varying heading of the UAV and derived corresponding channel statistics. [23] was the first to investigate the impact of UAV rotation on channel non-stationarity, and simulations demonstrated that UAV rotation significantly affects channel statistical characteristics and non-stationarity.

However, in the aforementioned channel model, such as in reference [21], only the transmitting and receiving nodes during UAV communication are considered, neglecting the objective scenario where non-communication nodes, present in multi-node UAV swarm, may traverse the channel between the two communicating nodes and cause interference. Therefore, further research is needed for UAV swarm multi-node channel models.

In response to the aforementioned issues, this paper primarily investigates the channel modeling of UAV swarm communication based on non-communication nodes. This model offers insights into performance evaluation and validation of UAV swarm communication systems. The main contributions of this paper are as follows:

1) This paper proposes a wideband non-stationary channel model for UAV swarm communication. The model comprises line-of-sight (LOS), single-bounce components, and double- bounce components. Furthermore, to accurately describe the UAV swarm communication scenario, heterogeneous scatterers are employed, with dual spheroids representing near-end scatterers and a cylinder representing far-end scatterers.

2) The proposed model takes into account not only the impact of the motion state of the Transmitting Node (TN) on the channel but also the influence of the motion state of the non-communication Node (NC) on the channel.

3) In the proposed model, the velocity of the UAV swarm, inter-UAV distances, departure and arrival angles are considered as time-varying parameters. Time-varying spatial -temporal-frequency correlation functions(S-T-FCF) and time-varying Doppler power spectral density(DPSD) are derived as channel statistical characteristics and validated through simulations. The simulation results demonstrate that the statistical characteristics of the multi-node wideband UAV channel model are generally similar to existing models, but the impact of non-communication nodes on these statistical characteristics cannot be ignored.

The rest of this paper is organized as follows. Section 2 provides a detailed introduction to the wideband non-stationary MIMO channel model for UAV swarm communication. Section 3 derives the transfer functions, spatial -temporal-frequency correlation functions, and Doppler power spectral density. Section 4 analyzes the numerical results. Finally, Section 5 presents the conclusion.

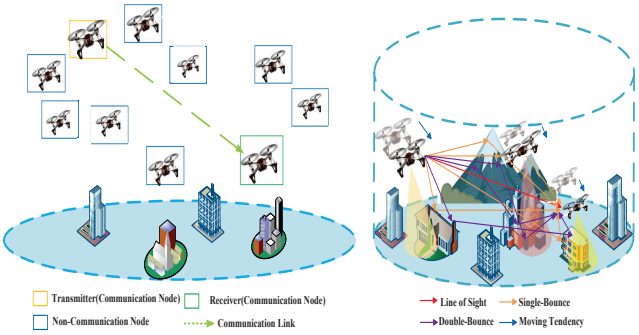

Fig. 1 UAV swarm Communication Scenario.
The left image illustrates the classification of UAV nodes, while the right image depicts the communication paths among UAVs.

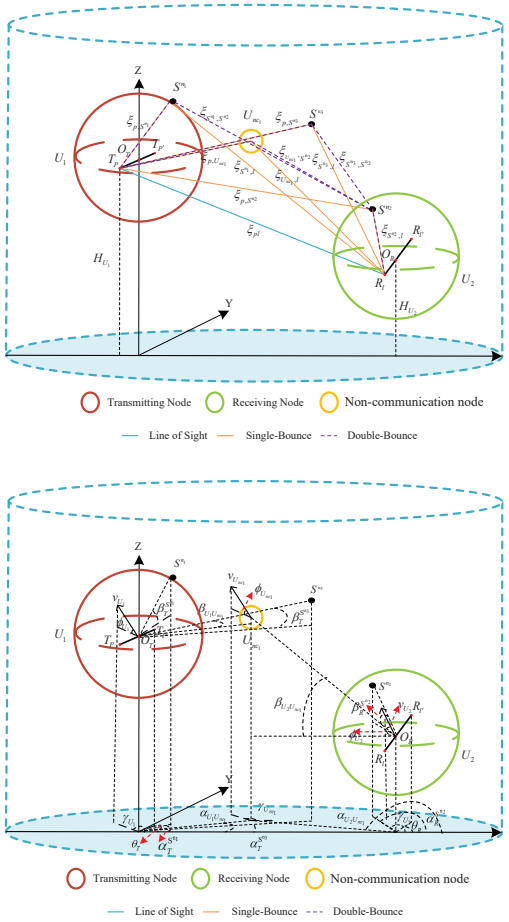

Fig. 2 UAV swarm Communication Scenario
The upper diagram shows the schematic diagram of UAV communication signal transmission paths, while the lower diagram illustrates the angles of UAV communication signal transmission.

2. Channel Model

2.1 Theoretical Model

Assuming there are N UAVs engaged in collaborative tasks in

Table 1 Definitions of Channel Model Parameters

Parameter	Definition
$v_{U_1}, v_{U_2}, v_{nc_j}$	The velocities of U_1,U_2 and U_{nc_j}
$\gamma_{U_1}, \gamma_{U_2}, \gamma_{U_{nc_j}}$	The azimuth angle of U_1, U_2 and U_{nc_j}
$\phi_{U_1}, \phi_{U_2}, \phi_{U_{nc_j}}$	The elevation angle of U_1, U_2 and U_{nc_j}
$D_{U_1U_2}, D_{U_1U_{nc_j}}, D_{U_2U_{nc_j}}$	The relative distances on the horizontal plane between U_1 to U_2, U_1 to U_{nc_j}, and U_2 to U_{nc_j}
$V\mathrm{d}_{U_{nc_j}}$	The vertical distance from U_{nc_j} to the line connecting U_1 and U_2
$\alpha_{U_1U_{nc_j}}, \beta_{U_1U_{nc_j}}$	The relative azimuth angle and relative elevation angle of U_1 and U_{nc_j}
$\alpha_{U_2U_{nc_j}}, \beta_{U_2U_{nc_j}}$	The relative azimuth angle and relative elevation angle of U_2 and U_{nc_j}
$\alpha_T^{S^{n_1}}, \beta_T^{S^{n_1}}, \alpha_R^{S^{n_1}}, \beta_R^{S^{n_1}}$	Elevation and azimuth angles from the transmitting node to S^{n_1} . Elevation and azimuth angles from S^{n_1} to the receiving node
$\alpha_T^{S^{n_2}}, \beta_T^{S^{n_2}}, \alpha_R^{S^{n_2}}, \beta_R^{S^{n_2}}$	Elevation and azimuth angles from the transmitting node to S^{n_2} . Elevation and azimuth angles from S^{n_2} to the receiving node
$\alpha_T^{S^{n_3}}, \beta_T^{S^{n_3}}, \alpha_R^{S^{n_3}}, \beta_R^{S^{n_3}}$	Elevation and azimuth angles from the transmitting node to S^{n_3} . Elevation and azimuth angles from S^{n_3} to the receiving node
N	The number of UAVs

the UAV swarm, when UAVs communicate, the transmitting and receiving nodes are denoted as U_1 and U_2 respectively. Other UAVs in the swarm not participating in this communication event are referred to as non-communicating nodes. The multi-node communication scenario in the UAV swarm is illustrated in Figure 1.The heterogeneous scatterers considered in this paper consist of two parts: distant scatterers, representing tall buildings and mountains in the distance, and proximal scatterers located near the transmitting and receiving nodes, representing nearby residential areas and small hills.Assuming a large number of scatterers are distributed around the signal transmission node and the signal reception node, each located on spheres with radii R_1 and R_2 respectively. At the transmitting node, there are N_1 scatterers, with the n_1th scatterer denoted as $S^{n_1}, n_1 = (1 \cdots N_1)$; at the receiving node, there are N_2 scatterers, with the n_2th scatterer denoted as $S^{n_2}, n_2 = (1 \cdots N_2)$. Distant scatterers, totaling N_3 , are distributed along the lateral surface of a cylinder with a radius of R_3 , with the n_3th scatterer denoted as $S^{n_3}, n_3 = (1 \cdots N_3)$ .In this model, the antennas at the transmitting and receiving nodes both employ omnidirectional reception antennas with low elevation angle uniform linear arrays. The number of elements in the transmitting antenna array is denoted as N_T , and the number of elements in the receiving antenna array is denoted as N_R. The orientations of the antennas are respectively labeled as θ_T and θ_R.T_P and $T_P^{'}$ represent the pth and $p^{'}$th antennas of U_1 , with the center point at O_T and antenna spacing of δ_T .R_l and $R_l^{'}$ represent the lth and $l^{'}$th antennas of U_2 , with the center point atO_R and antenna spacing of δ_R.The heights of UAVs U_1, U_2 and U_{nc_j} are H_{U_1} , H_{U_2} , and H_{nc_j} , respectively.The other relevant parameters and their definitions are shown in Table 1 below.

2.2 Channel Impulse Response

Based on the GBSM depicted in Figure 2, two different components are considered for the UAV swarm communication environment: Line-of-Sight (LoS) component, where the wave from the transmitting node can directly propagate to the receiving node, and Non-Line-of-Sight (NLOS) component, which includes single-bounce and double-bounce [21]. The single-bounce reflections consist of SB_1, where the signal scatters off a scatterer near the transmitting node before reaching the receiving node; SB_2, where the signal scatters off a scatterer near the receiving node before reaching the receiving node; SB_3, where the signal scatters off a scatterer far from both the transmitting and receiving nodes before reaching the receiving node; SB_{nc}, where the signal scatters off non-communicating nodes within the swarm before reaching the receiving node. The double-bounce reflections consist of DB_1, where the signal bounces off one scatterer before bouncing off another scatterer before reaching the receiving node; DB_2, where the signal bounces off one scatterer before bouncing off another scatterer before reaching the receiving node; DB_{nc}, where the channel bounces off non-communicating nodes before bouncing off a scatterer before reaching the receiving node. Thus, the channel impulse response of the UAV swarm communication link can be written as the summation of the LoS component and the NLOS components, i.e.,

$$h_{pl}(t_i, \tau) = h_{pl}^{Los}(t_i, \tau) + h_{pl}^{NLos}(t_i, \tau), \tag{1}$$

$$h_{pl}^{NLos}(t_i, \tau) = h_{pl}^{SB}(t_i, \tau) + h_{pl}^{DB}(t_i, \tau), \tag{2}$$

where $h_{pl}^{Los}(t_i, \tau)$ and $h_{pl}^{NLos}(t_i, \tau)$ represent the channel impulse responses of the LoS component and NLOS component, respectively, while $h_{pl}^{SB}(t_i, \tau)$ and $h_{pl}^{DB}(t_i, \tau)$ de-

note the channel impulse responses of single-bounce(SB) and double-bounce(DB) reflections. The expansions of each term are as follows.

$$h_{pl}^{Los}(t_i,\tau) = \sqrt{\frac{K\Omega_{pl}}{K+1}} \times \exp\left(-j\frac{2\pi}{\lambda}\xi_{pl}(t_i)\right) \times \exp(j2\pi f_{Los}(t_i)\times t_i) \times \delta\left(\tau - \tau_{Los}(t_i)\right), \tag{3}$$

where K represents the Rayleigh factor; Ω_{pl} denotes the energy from p to l; λ is the carrier wavelength; the derivation process of the transmission distance $\xi_{pl}(t_i)$, Doppler frequency shift $f_{Los}(t_i)$, and propagation delay $\tau_{Los}(t_i)$ can be found in APPENDIX A.

$$\begin{aligned} h_{pl}^{SB}(t_i,\tau) &= \sum_{a=1}^{3} h_{pl}^{SB_a}(t_i,\tau) + \tilde{h}_{pl}^{SB_{nc}}(t_i,\tau) = \\ &\sum_{a=1}^{3} \sqrt{\frac{\eta_{SB_a}\Omega_{pl}}{K+1}} \lim_{N_a\to\infty} \sum_{n_a=1}^{N_a} \frac{1}{\sqrt{N_a}} \times \exp\left(-j\frac{2\pi}{\lambda}\xi_{SB_a}(t_i)\right) \\ &\times \exp\left(j2\pi f_{SB_a}(t_i)\times t_i\right) \times \delta\left(\tau - \tau_{SB_a}(t_i)\right) \\ &+ \sum_{j=1}^{N-2} \sqrt{\frac{\eta_{SB_{nc_j}}\Omega_{pl}}{K+1}} \times \exp\left(-j\frac{2\pi}{\lambda}\xi_{SB_{nc_j}}(t_i)\right) \\ &\times \exp\left(j2\pi f_{SB_{nc_j}}(t_i)\times t_i\right) \times \delta\left(\tau - \tau_{SB_{nc_j}}(t_i)\right). \end{aligned} \tag{4}$$

The above equation represents the channel impulse response of single-bounce reflections in the NLOS component.Where $\sum_{a=1}^{3} h_{pl}^{SB_a}(t_i,\tau)$ denotes the sum of the channel impulse responses of SB_1, SB_2, and SB_3, while $\tilde{h}_{pl}^{SB_{nc}}(t_i,\tau)$ represents the channel impulse response of SB_{nc},and $SB_{nc} = \sum_{j=1}^{N-2} SB_{nc_j}$. $\eta_{SB_1}, \eta_{SB_2}, \eta_{SB_3}, \sum_{j=1}^{N-2} \eta_{SB_{nc_j}}$ represents the proportion of energy of each component in the SB reflections to the total energy; the derivation process of the transmission distances $\xi_{SB_a}(t_i), a = 1,2,3$ and $\xi_{SB_{nc_j}}(t_i), j = 1,\cdots,N-2$, Doppler frequency shifts $f_{SB_a}(t_i), a = 1,2,3$ and $f_{SB_{nc_j}}(t_i), j = 1,\cdots,N-2$, and propagation delays $\tau_{SB_a}(t_i), a = 1,2,3$ and $\tau_{SB_{nc_j}}(t_i), j = 1,\cdots,N-2$ can be found in APPENDIX B.

$$\begin{aligned} h_{pl}^{DB}(t_i,\tau) &= h_{pl}^{DB_1}(t_i,\tau) + h_{pl}^{DB_2}(t_i,\tau) + \tilde{h}_{pl}^{DB_{nc}}(t_i,\tau) = \\ &\sqrt{\frac{\eta_{DB_1}\Omega_{pl}}{K+1}} \lim_{N_1,N_2\to\infty} \sum_{n_1,n_2=1}^{N_1,N_2} \frac{1}{\sqrt{N_1N_2}} \times \exp\left(-j\frac{2\pi}{\lambda}\xi_{DB_1}(t_i)\right) \\ &\times \exp\left(j2\pi f_{DB_1}(t_i)\times t_i\right) \times \delta\left(\tau - \tau_{DB_1}(t_i)\right) + \\ &\sqrt{\frac{\eta_{DB_2}\Omega_{pl}}{K+1}} \lim_{N_2,N_3\to\infty} \sum_{n_2,n_3=1}^{N_2,N_3} \frac{1}{\sqrt{N_2N_3}} \times \exp\left(-j\frac{2\pi}{\lambda}\xi_{DB_2}(t_i)\right) \\ &\times \exp\left(j2\pi f_{DB_2}(t_i)\times t_i\right) \times \delta\left(\tau - \tau_{DB_2}(t_i)\right) + \\ &\sum_{j=1}^{N-2} \sqrt{\frac{\eta_{DB_{nc_j}}\Omega_{pl}}{K+1}} \lim_{N_2\to\infty} \sum_{n_2=1}^{N_2} \frac{1}{\sqrt{N_2}} \times \exp\left(-j\frac{2\pi}{\lambda}\xi_{DB_{nc_j}}(t_i)\right) \\ &\times \exp\left(j2\pi f_{DB_{nc_j}}(t_i)\times t_i\right) \times \delta\left(\tau - \tau_{DB_{nc_j}}(t_i)\right). \end{aligned} \tag{5}$$

The above equation represents the channel impulse response of double-bounce reflections in the NLOS component, $h_{pl}^{DB_1}(t_i,\tau)$,$h_{pl}^{DB_2}(t_i,\tau)$ and $\tilde{h}_{pl}^{DB_{nc}}(t_i,\tau)$ denote the channel impulse responses of DB_1, DB_2, and DB_{nc},respectively,and $DB_{nc} = \sum_{j=1}^{N-2} DB_{nc_j}$.The derivation process of the transmission distances $\xi_{DB_1}(t_i)$,$\xi_{DB_2}(t_i)$ and $\xi_{DB_{nc_j}}(t_i), j = 1,\cdots,N-2$, Doppler frequency shifts $f_{DB_1}(t_i)$, $f_{DB_2}(t_i)$ and $f_{DB_{nc_j}}(t_i), j = 1,\cdots,N-2$, and propagation delays $\tau_{DB_1}(t_i)$,$\tau_{DB_2}(t_i)$ and $\tau_{DB_{nc_j}}(t_i), j = 1,\cdots,N-2$ can be found in APPENDIX C. η_{DB_1}, η_{DB_2} and $\sum_{j=1}^{N-2} \eta_{DB_{nc_j}}$ represent the proportions of energy of each component in the DB reflections to the total energy, and satisfy $\eta_{SB_1}+\eta_{SB_2}+\eta_{SB_3}+\sum_{j=1}^{N-2}\eta_{SB_{nc_j}}+\eta_{DB_1}+\eta_{DB_2}+\sum_{j=1}^{N-2}\eta_{DB_{nc_j}} = 1$.

In non-stationary communication scenarios, the statistical characteristics of the channel change over time. To depict the non-stationary nature of the channel, the introduction of time-varying parameters is of significant importance. In this section, the UAV's mobile velocity, inter-UAV distance parameters, as well as departure and arrival angles are considered as time-varying parameters.Further detailed parameter derivations can be found in the appendix.

In the proposed model, it is assumed that the number of scatterers is infinitely large, i.e., $N_1N_2N_3 \to \infty$. Therefore, the discrete azimuth angle $\alpha_{T/R}^{S^{na}}(a = 1,2,3)$and elevation angle $\beta_{T/R}^{S^{na}}(a = 1,2,3)$ are represented by continuous random variables $\alpha_{T/R}$ and $\beta_{T/R}$ with given probability density functions.

For the probability density function of the azimuth angle, referencing previous research literature, this paper adopts the von Mises-Fisher distribution (VMF) to characterize it:

$$f(\alpha) = \frac{e^{k\cos(\alpha-\alpha_\mu)}}{2\pi I_0(k)}, \alpha \in [-\pi,\pi], \tag{6}$$

where $I_0(\bullet)$ represents the first-kind zero-order modified Bessel function, α_μ is the angular mean, and k indicates the extent of scatter around the mean for the scatterers.

For the probability density function of the elevation angle, referencing previous research literature, this paper adopts the cosine distribution for representation:

$$f(\beta) = \frac{\pi}{4\beta_n}\cos\left(\frac{\pi}{2}\frac{\beta-\beta_\mu}{\beta_n}\right), \tag{7}$$

where $\beta \in \left[\beta_\mu - \beta_n, \beta_\mu + \beta_n\right]$,$\left|\beta - \beta_\mu\right| \le |\beta_n| \le \frac{\pi}{2}$. Parameter β_μ is the central angle of angle β, and β_n is the maximum offset.

3. Statistical characteristics analysis of the channel reference model

3.1 Spatial-Temporal-Frequency Correlation Function

By Fourier transforming the obtained channel impulse response with respect to the propagation delay τ, the channel impulse response can be converted from the time domain to the frequency domain, the transfer function can be obtained.

$$\begin{aligned} H_{pl}(t_i,f) &= H_{pl}^{Los}(t_i,f) + H_{pl}^{NLos}(t_i,f) \\ &= H_{pl}^{Los}(t_i,f) + H_{pl}^{SB}(t_i,f) + H_{pl}^{DB}(t_i,f), \end{aligned} \tag{8}$$

where,

$$\begin{aligned} &H_{pl}^{Los}(t_i,f) = \sqrt{\frac{K\Omega_{pl}}{K+1}} \times \exp(-j\frac{2\pi}{\lambda}\xi_{pl}(t_i)) \\ &\times \exp(j2\pi f_{Los}(t_i) \times t_i) \times \exp(-j2\pi f \tau_{Los}(t_i)), \end{aligned} \tag{9}$$

$$\begin{aligned} &H_{pl}^{SB}(t_i,f) = \sum_{a=1}^{3} H_{pl}^{SB_a}(t_i,f) + \tilde{H}_{pl}^{SB_{nc}}(t_i,f) = \\ &\sum_{a=1}^{3} \sqrt{\frac{\eta_{SB_a}\Omega_{pl}}{K+1}} \lim_{N_a\to\infty} \sum_{n_a=1}^{N_a} \frac{1}{\sqrt{N_a}} \times \exp(-j\frac{2\pi}{\lambda}\xi_{SB_a}(t_i)) \\ &\times \exp(j2\pi f_{SB_a}(t_i) \times t_i) \times \exp(-j2\pi f \tau_{SB_a} t_i) \\ &+ \sum_{nc_j=1}^{N-2} \sqrt{\frac{\eta_{SB_{nc_j}}\Omega_{pl}}{K+1}} \times \exp(-j\frac{2\pi}{\lambda}\xi_{SB_{nc_j}}(t_i)) \\ &\times \exp(j2\pi f_{SB_{nc_j}}(t_i) \times t_i) \times \exp(-j2\pi f \tau_{SB_{nc_j}}(t_i)), \end{aligned} \tag{10}$$

$$\begin{aligned} &H_{pl}^{DB}(t_i,f) = H_{pl}^{DB_1}(t_i,f) + H_{pl}^{DB_2}(t_i,f) + \tilde{H}_{pl}^{DB_{\mathrm{nc}}}(t_i,f) = \\ &\sqrt{\frac{\eta_{DB_1}\Omega_{pl}}{K+1}} \lim_{N_1,N_2\to\infty} \sum_{n_1,n_2=1}^{N_1,N_2} \frac{1}{\sqrt{N_1 N_2}} \times \exp(-j\frac{2\pi}{\lambda}\xi_{DB_1}(t_i)) \\ &\times \exp(j2\pi f_{DB_1}(t_i) \times t_i) \times \exp(-j2\pi f \tau_{DB_1}(t_i)) \\ &+ \sqrt{\frac{\eta_{DB_2}\Omega_{pl}}{K+1}} \lim_{N_2,N_3\to\infty} \sum_{n_2,n_3=1}^{N_2,N_3} \frac{1}{\sqrt{N_2 N_3}} \times \exp(-j\frac{2\pi}{\lambda}\xi_{DB_2}(t_i)) \\ &\times \exp(j2\pi f_{DB_2}(t_i) \times t_i) \times \exp(-j2\pi f \tau_{DB_2}(t_i)) \\ &+ \sum_{nc_j=1}^{N-2} \sqrt{\frac{\eta_{DB_{nc_j}}\Omega_{pl}}{K+1}} \lim_{N_2\to\infty} \sum_{n_2=1}^{N_2} \frac{1}{\sqrt{N_2}} \times \exp(-j\frac{2\pi}{\lambda}\xi_{DB_{nc_j}}(t_i)) \\ &\times \exp(j2\pi f_{DB_{nc_j}}(t_i) \times t_i) \times \exp(-j2\pi f \tau_{DB_{nc_j}}(t_i)), \end{aligned} \tag{11}$$

where $H_{pl}^{SB_a}(t_i,f), a = 1,2,3, H_{pl}^{DB_1}(t_i,f)$, and $H_{pl}^{DB_2}(t_i,f)$ represent the components related to the scatterers. $\tilde{H}_{pl}^{SB_{\mathrm{nc}}}(t_i,f)$ and $\tilde{H}_{pl}^{DB_{\mathrm{nc}}}(t_i,f)$represent the components related to non-communication nodes.

After obtaining the transfer function, we can compute the channel statistical characteristics of the UAV swarm communication channel.The Spatial-Temporal-Frequency Correlation Function(S-T-F-CF) between two arbitrary channel impulse responses $H_{pl}(t_i,f)$and$H_{p'l'}(t_i,f)$ is defined as:

$$\begin{aligned} &R_{pl,p'l'}(\delta_T,\delta_R,t_i,\Delta t,f,\Delta f) \\ &= \frac{E\left[H_{pl}(t_i,f)H_{p'l'}^{*}(t_i+\Delta t,f+\Delta f)\right]}{\sqrt{\Omega_{pl}\Omega_{p'l'}}}, \end{aligned} \tag{12}$$

where $(.)^*$ represents the complex conjugate, and $E[.]$ denotes taking the expectation. Since the LOS, SB, and DB components are complex Gaussian random processes with zero mean, the above equation can be written as:

$$\begin{aligned} &R_{pl,p'l'}(\delta_T,\delta_R,t_i,\Delta t,f,\Delta f) \\ &= R_{pl,p'l'}^{Los}(\delta_T,\delta_R,t_i,\Delta t,f,\Delta f) \\ &+ R_{pl,p'l'}^{SB}(\delta_T,\delta_R,t_i,\Delta t,f,\Delta f) \\ &+ R_{pl,p'l'}^{DB}(\delta_T,\delta_R,t_i,\Delta t,f,\Delta f), \end{aligned} \tag{13}$$

when $\Delta t, \Delta f = 0$, the spatial correlation function can be obtained; when $\delta_T, \delta_R, \Delta f = 0$, the temporal correlation function can be obtained; and when $\delta_T, \delta_R, \Delta t = 0$, the frequency correlation function can be obtained. The components in the equation are defined as follows:

$$\begin{aligned} &R_{pl,p'l'}^{Los}(\delta_T,\delta_R,t_i,\Delta t,f,\Delta f) \\ &= \frac{K}{K+1} \times \exp(-j\frac{2\pi}{\lambda}(\xi_{pl}(t_i) - \xi_{p'l'}(t_i))) \\ &\times \exp(-j2\pi f_{Los}(t_i)\Delta t) \times \exp(j2\pi\Delta f \tau_{Los}(t_i)), \end{aligned} \tag{14}$$

$$\begin{aligned} &R_{pl,p'l'}^{SB}(\delta_T,\delta_R,t_i,\Delta t,f,\Delta f) = \\ &\frac{\eta_{SB_1}}{K+1} \int_{-\pi}^{\pi} \int_{\beta_{T\mu}^{S^{n_1}} - \beta_{Tn}^{S^{n_1}}}^{\beta_{T\mu}^{S^{n_1}} + \beta_{Tn}^{S^{n_1}}} f(\alpha_T^{S^{n_1}}) f\left(\beta_T^{S^{n_1}}\right) \\ &\times \exp(-j\frac{2\pi}{\lambda}\left(\xi_{SB_1}(t_i) - \xi'_{SB_1}(t_i)\right)) \\ &\times \exp(-j2\pi f_{SB_1}(t_i)\Delta t) \times \exp(j2\pi\Delta f \tau_{SB_1}(t_i)) \\ &d\alpha_T^{S^{n_1}} d\beta_T^{S^{n_1}} + \frac{\eta_{SB_2}}{K+1} \int_{-\pi}^{\pi} \int_{\beta_{R\mu}^{S^{n_2}} - \beta_{Rn}^{S^{n_2}}}^{\beta_{R\mu}^{S^{n_2}} + \beta_{Rn}^{S^{n_2}}} f(\alpha_R^{S^{n_2}}) f\left(\beta_R^{S^{n_2}}\right) \\ &\times \exp(-j\frac{2\pi}{\lambda}\left(\xi_{SB_2}(t_i) - \xi'_{SB_2}(t_i)\right)) \times \exp(-j2\pi f_{SB_2}(t_i)\Delta t) \\ &\times \exp(j2\pi\Delta f \tau_{SB_2}(t_i)) d\alpha_R^{S^{n_2}} d\beta_R^{S^{n_2}} \\ &+ \frac{\eta_{SB_3}}{K+1} \int_{-\pi}^{\pi} \int_{\beta_{T\mu}^{S^{n_3}} - \beta_{Tn}^{S^{n_3}}}^{\beta_{T\mu}^{S^{n_3}} + \beta_{Tn}^{S^{n_3}}} f(\alpha_T^{S^{n_3}}) f\left(\beta_T^{S^{n_3}}\right) \\ &\times \exp(-j\frac{2\pi}{\lambda}\left(\xi_{SB_3}(t_i) - \xi'_{SB_3}(t_i)\right)) \\ &\times \exp(-j2\pi f_{SB_3}(t_i)\Delta t) \times \exp(j2\pi\Delta f \tau_{SB_3}(t_i)) d\alpha_T^{S^{n_3}} d\beta_T^{S^{n_3}} \\ &+ \sum_{nc_j=1}^{N-2} \frac{\eta_{SB_{nc_j}}}{K+1} \times \exp(-j\frac{2\pi}{\lambda}\left(\xi_{SB_{nc_j}}(t_i) - \xi'_{SB_{nc_j}}(t_i)\right)) \\ &\times \exp(-j2\pi f_{SB_{nc_j}}(t_i)\Delta t) \times \exp(j2\pi\Delta f \tau_{SB_{nc_j}}(t_i)), \end{aligned} \tag{15}$$

$$\begin{aligned} &R_{pl,p'l'}^{DB}(\delta_T,\delta_R,t_i,\Delta t,f,\Delta f) = \\ &\frac{\eta_{DB_1}}{K+1} \int_{-\pi}^{\pi} \int_{\beta_{T\mu}^{S^{n_1}} - \beta_{Tn}^{S^{n_1}}}^{\beta_{T\mu}^{S^{n_1}} + \beta_{Tn}^{S^{n_1}}} \int_{-\pi}^{\pi} \int_{\beta_{R\mu}^{S^{n_2}} - \beta_{Rn}^{S^{n_2}}}^{\beta_{R\mu}^{S^{n_2}} + \beta_{Rn}^{S^{n_2}}} f(\alpha_T^{S^{n_1}}) f\left(\beta_T^{S^{n_1}}\right) \\ &f(\alpha_R^{S^{n_2}}) f\left(\beta_R^{S^{n_2}}\right) \times \exp(-j\frac{2\pi}{\lambda}\left(\xi_{DB_1}(t_i) - \xi'_{DB_1}(t_i)\right)) \\ &\times \exp(-j2\pi f_{DB_1}(t_i)\Delta t) \times \exp(j2\pi\Delta f \tau_{DB1}(t_i)) \\ &\times d\alpha_T^{S^{n_1}} d\beta_T^{S^{n_1}} d\alpha_R^{S^{n_2}} d\beta_R^{S^{n_2}} + \frac{\eta_{DB_2}}{K+1} \int_{-\pi}^{\pi} \int_{\beta_{T\mu}^{S^{n_3}} - \beta_{Tn}^{S^{n_3}}}^{\beta_{T\mu}^{S^{n_3}} + \beta_{Tn}^{S^{n_3}}} \\ &\int_{-\pi}^{\pi} \int_{\beta_{R\mu}^{S^{n_2}} - \beta_{Rn}^{S^{n_2}}}^{\beta_{R\mu}^{S^{n_2}} + \beta_{Rn}^{S^{n_2}}} f(\alpha_T^{S^{n_3}}) f\left(\beta_T^{S^{n_3}}\right) f\left(\alpha_R^{S^{n_2}}\right) f\left(\beta_R^{S^{n_2}}\right) \\ &\times \exp(-j\frac{2\pi}{\lambda}\left(\xi_{DB_2}(t_i) - \xi'_{DB_2}(t_i)\right)) \\ &\times \exp(-j2\pi f_{DB_2}(t_i)\Delta t) \times \exp(j2\pi\Delta f \tau_{DB2}(t_i)) \\ &\times d\alpha_T^{S^{n_3}} d\beta_T^{S^{n_3}} d\alpha_R^{S^{n_2}} d\beta_R^{S^{n_2}} \\ &+ \sum_{nc_j=1}^{N-2} \frac{\eta_{DB_{nc_j}}}{K+1} \int_{-\pi}^{\pi} \int_{\beta_{R\mu}^{S^{n_2}} - \beta_{Rn}^{S^{n_2}}}^{\beta_{R\mu}^{S^{n_2}} + \beta_{Rn}^{S^{n_2}}} f(\alpha_R^{S^{n_2}}) f\left(\beta_R^{S^{n_2}}\right) \\ &\times \exp(-j\frac{2\pi}{\lambda}\left(\xi_{DB_{nc_j}}(t_i) - \xi'_{DB_{nc_j}}(t_i)\right)) \end{aligned}$$

Table 2 Channel Model Simulation Parameters

Parameters	Values	Parameters	Values
UAV communication center frequency (GHz)	2.4 GHz	θ_T, θ_R	$\pi/3, \pi/4$
$v_{U_1}, v_{U_2}, v_{U_{nc_1}}$ (m/s)	60, 60, 50(m/s)	$\gamma_{U_1}, \gamma_{U_2}, \gamma_{U_{nc_1}}$	$\pi/6, \pi/4, \pi/6$
$\phi_{U_1}, \phi_{U_2}, \phi_{U_{nc_1}}$	$\pi/6, \pi/4, \pi/12$	$D_{U_1U_2}, D_{U_1U_{nc_1}}, D_{U_2U_{nc_1}}$ (m)	200, 140, 60(m)
$Vd_{U_{nc_1}}$ (m)	140(m)	$\alpha_{T\mu}^{S^{n_1}}, \alpha_{R\mu}^{S^{n_2}}, \alpha_{T\mu}^{S^{n_3}}$	$\pi/3, \pi/3, \pi/3$
$\beta_{T\mu}^{S^{n_1}}, \beta_{R\mu}^{S^{n_2}}, \beta_{T\mu}^{S^{n_3}}$	$\pi/6, \pi/6, \pi/6$	K(dB)	1(dB)
$H_{U_1}, H_{U_2}, H_{U_{nc_1}}$ (m)	160, 70, 100(m)	$a_{UAV_1}, a_{UAV_2}, a_{UAV_{nc_1}}$ (m/s)	1, 1, 1(m/s)

$$\times \exp(-j2\pi f_{DB_{nc_j}}(t_i)\,\Delta t) \times \exp(j2\pi\Delta f \tau_{DB_{nc_j}}(t_i)) d\alpha_R^{S^{n_2}}\, d\beta_R^{S^{n_2}}, \tag{16}$$

3.2 Doppler power spectral density

The obtained temporal autocorrelation function $R_{pl,p'l'}(\Delta t)$ can be transformed using the Fourier transform to derive the corresponding Doppler power spectral density:

$$S_{pl,p'l'}(f_D) = \int_{-\infty}^{+\infty} R_{pl,p'l'}(\Delta t)\exp(-j2\pi f_D \Delta t), \tag{17}$$

where,

$$S_{pl,p'l'}(f_D) = S_{pl,p'l'}^{Los}(f_D) + S_{pl,p'l'}^{SB}(f_D) + S_{pl,p'l'}^{DB}(f_D). \tag{18}$$

4. Numerical Analysis and Validation

In this section, numerical analysis will be employed to investigate the impact of UAV swarm motion parameters on the channel statistical characteristics, such as the spatial -temporal-frequency correlation functions and the time-varying Doppler power spectral density. Unless otherwise specified, the simulations use the parameters listed in Table 2.To reduce simulation time, the number of UAVs in the swarm N is set to three.

4.1 Analysis of the SCF results

The spatial correlation functions at different moments were initially analyzed. From Figure 3, it can be observed that the spatial correlation functions vary at different instances. Specifically, the spatial correlation decreases with an increase in the antenna spacing of the transmitting nodes. Additionally, the spatial correlation is highest at t=0s, and as t increases, the spatial correlation gradually decreases. The varying shapes of the spatial correlation function at different moments indicate that the proposed model is capable of capturing the non-stationarity of the UAV swarm communication channel.

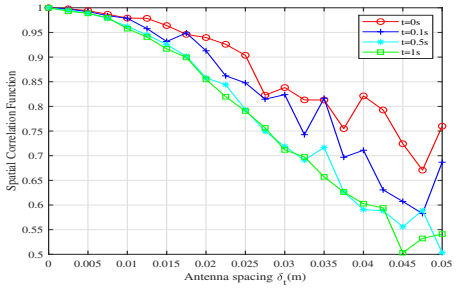

Fig. 3 Spatial Correlation Functions at Different Moments

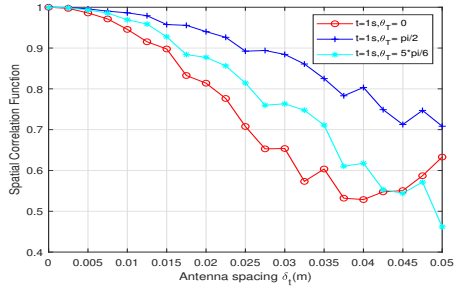

Fig. 4 The impact of the transmitting node's movement velocity on the TCF

Figure 4 illustrates the spatial correlation functions at different transmitting node antenna azimuth angles when t=1s. It can be observed that, when the transmitting antenna azimuth angle is $\left[0, \frac{\pi}{2}\right]$, the spatial correlation increases with the azimuth angle; for transmitting node antenna azimuth angle $\frac{\pi}{2}$, the maximum spatial correlation is obtained, as evident from the graph, which indicates an increase of 0.29 compared to the minimum value; while for transmitting node antenna azimuth angle $\left[\frac{\pi}{2}, \pi\right]$, the spatial correlation decreases with the azimuth angle.

Figures 5 and 6 depict the influence of mobile azimuth angles on the spatial correlation functions at t=1s. Figure 5 examines the effect of transmitting node mobile azimuth angles, demonstrating consistent trends in spatial correlation—greater antenna spacing leads to lower spatial correlation, and at the same antenna spacing, larger angles result in higher spatial correlation. Figure 6 investigates the impact of non-communication node mobile azimuth angles on spa-

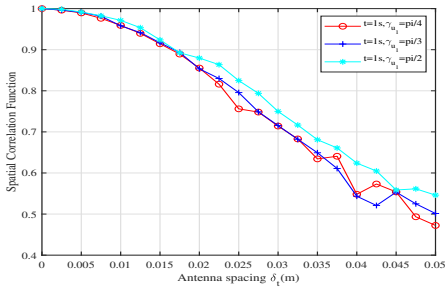

Fig. 5 Spatial Correlation Functions at Different Transmitting Node Mobile Azimuth Angles

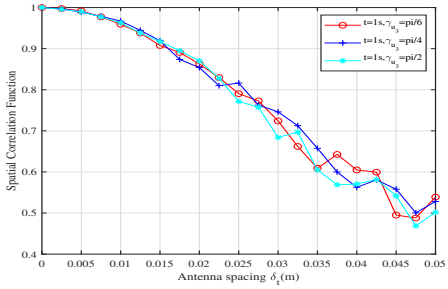

Fig. 6 Spatial Correlation Functions at Different non-communication Node Mobile Azimuth Angles

tial correlation functions. The plot in Figure 6 shows that with changes in the mobile azimuth angle, the trend in correlation alteration remains uniform, and the correlations are similar, with a maximum correlation of only 0.04. This indicates that the influence of non-communication node mobile azimuth angles on spatial correlation can be negligible.

In summary, Figures 3 to 6 investigate the impact of channel correlation parameters on spatial correlation functions. Specifically, Figures 3 to 5 examine the influence of the channel parameters proposed in reference [21] on spatial correlation functions. From the figures, it can be observed that the proposed model exhibits a generally similar trend to the known models, where the spatial correlation functions decrease as the spacing between transmitting node elements increases. Furthermore, for the same element spacing, both the transmitting node antenna azimuth angle and the mobile azimuth angle have a significant impact on spatial correlation functions, leading to an increase in spatial correlation. Figure 6 explores the effect of non-communication node mobile azimuth angles on spatial correlation functions, indicating that changes in angle have a negligible impact on spatial correlation functions.

4.2 Analysis of the TCF results

From Figure 7, it can be observed that the temporal autocorrelation function curves vary at different time instances. Specifically, when t=0s, the temporal correlation is highest, and as t increases, the temporal correlation decreases. This is due to the fact that as time increases, the speed of the UAV swarm becomes faster, leading to increased non-stationarity in the communication channel of the swarm, resulting in reduced temporal correlation. The variation of temporal correlation with t also indicates the non-stationarity of the UAV swarm communication channel.

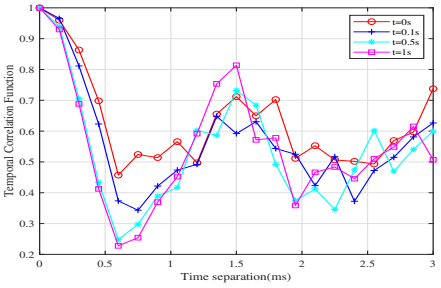

Fig. 7 Temporal Autocorrelation Functions at Different Time Instances

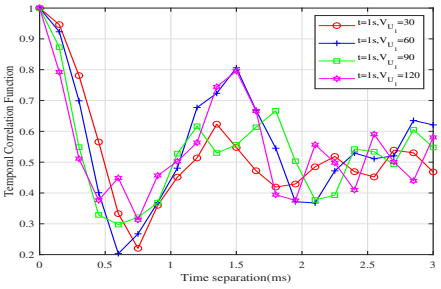

Fig. 8 Temporal Autocorrelation Functions at Different Transmitting Node Velocities

Figure 8 illustrates the variation of temporal autocorrelation functions at different transmitting node velocities. It can be observed that as the transmitting node velocity increases, the temporal autocorrelation function curve decreases. This is attributed to the unchanged velocity of the receiving node and the increased velocity of the transmitting node, which leads to variations in the Doppler frequency shift of the communication link, resulting in a decrease in the temporal autocorrelation function. Under the same time interval, the maximum variation in the temporal autocorrelation function can reach up to 0.27.

Figure 9 demonstrates the impact of non-communication node velocities on the temporal autocorrelation functions. From the graph, it can be observed that as the velocity of the non-communication nodes increases, the temporal autocorrelation function decreases. This is due to the excessive speed causing a significant Doppler frequency shift in the swarm, resulting in a decrease in the temporal autocorrelation function. Furthermore, it's evident that at low speeds, the variation in the temporal autocorrelation function is minimal and can be almost neglected. However, at higher speeds, the variation in the temporal autocorrelation function is much

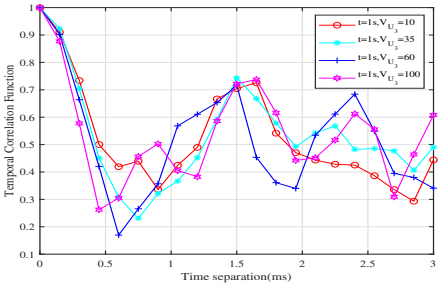

Fig. 9 Temporal Autocorrelation Functions at Different non-communication Node Mobile Velocities

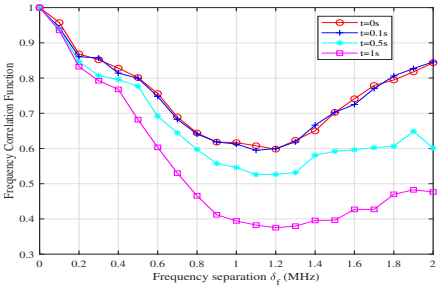

Fig. 10 Temporal Autocorrelation Functions at Different non-communication Node Mobile Velocities

larger. Under the same time interval, the maximum variation in the temporal autocorrelation function can reach up to 0.24.

Figures 7 to 9 investigate the influence of channel correlation parameters on temporal autocorrelation functions. Among them, Figures 7 to 8 examine the impact of the relevant channel parameters mentioned in the existing models [21] on temporal autocorrelation functions. Conclusions drawn from these results indicate that the proposed model and known models exhibit similar trends in temporal autocorrelation functions: temporal correlation varies with time; furthermore, temporal autocorrelation decreases steadily with increasing time intervals and eventually stabilizes around a specific value with minor fluctuations. It's also evident that, under the same time interval, the transmitting node's velocity significantly impacts the temporal autocorrelation function, with a maximum variation of up to 0.27. Figure 10 delves into the effect of non-communication node velocities on temporal autocorrelation functions, where the impact of non-communication node velocities on the temporal autocorrelation function is substantial, with a variation of up to 0.24. In summary, the impact of the proposed channel model's correlation parameters on temporal autocorrelation functions is similar to that of existing models. However, the influence of parameters related to non-communication nodes on temporal autocorrelation functions cannot be ignored. This has significant implications for future research on multi-node communication channels in UAV swarm scenarios.

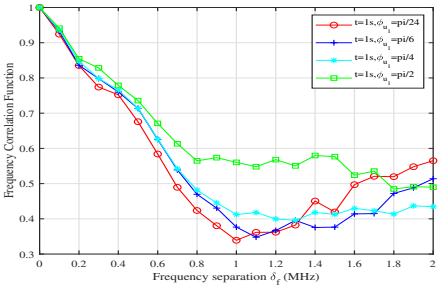

Fig. 11 Temporal Autocorrelation Functions at Different non-communication Node Mobile Velocities

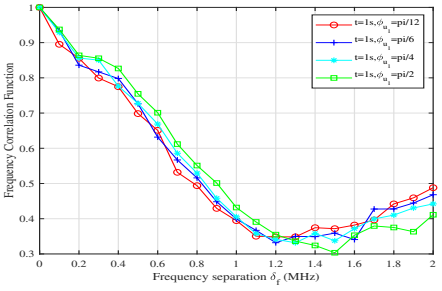

Fig. 12 Temporal Autocorrelation Functions at Different non-communication Node Mobile Velocities

4.3 Analysis of the FCF results

Figure 10 investigates the frequency autocorrelation functions at different time instances. From Figure 10, it can be observed that the frequency correlation decreases as the frequency increases, and as time progresses, the correlation continuously decreases. The distinct curves of frequency autocorrelation functions at different time instances underscore the non-stationarity of the communication channel within the swarm.

Figures 11 and 12 investigate the impact of mobile elevation angles on frequency autocorrelation functions. Figure 11 examines the influence of transmitting node mobile elevation angles, revealing that, under the same frequency interval, an increase in the transmitting node's mobile elevation angle corresponds to an increase in frequency correlation. Figure 12 explores the effect of non-communication node mobile elevation angles, demonstrating that within the same frequency interval, as the mobile elevation angle of non-communication nodes increases, the frequency autocorrelation function also increases, with a maximum variation of up to 0.1.

Figures 10 to 12 investigate the influence of channel correlation parameters on frequency autocorrelation functions. Among them, Figures 10 to 11 explore the effects of different time instances and transmitting node mobile elevation angles [21] on frequency autocorrelation functions. Conclusions drawn from these results indicate that temporal correlation varies continuously over time; furthermore,

frequency autocorrelation decreases steadily with increasing frequency intervals, eventually stabilizing around a specific value with minor fluctuations. Moreover, it is evident that, under the same frequency interval, the transmitting node's mobile elevation angle significantly affects frequency autocorrelation functions. Figure 12 delves into the effect of non-communication node mobile elevation angles, demonstrating a notable impact on frequency autocorrelation functions, with a maximum variation of up to 0.1. In summary, these findings underscore the non-negligible impact of non-communication nodes on frequency autocorrelation functions within the proposed model.

4.4 Analysis of the DPSD results

Figure 13 displays the Doppler Power Spectral Density (DPSD) at different time instances. It is evident from the figure that the power spectral density varies with time, a phenomenon attributed to the movement of the UAV swarm. The distinct variations in DPSD at different time instances underscore the non-stationarity of the communication channel within the swarm.

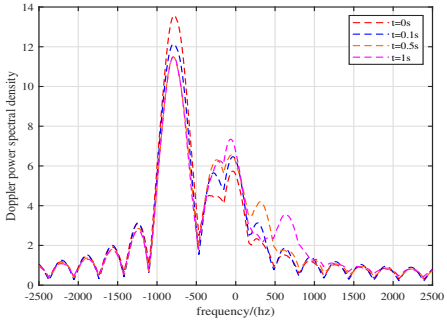

Fig. 13 Temporal Autocorrelation Functions at Different non-communication Node Mobile Velocities

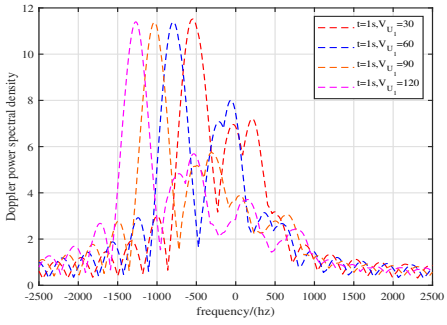

Fig. 14 Temporal Autocorrelation Functions at Different non-communication Node Mobile Velocities

Figures 14 and 15 investigate the influence of mobile velocities on Doppler Power Spectral Density. In Figure 14, the parameter under study is the transmitting node's velocity.

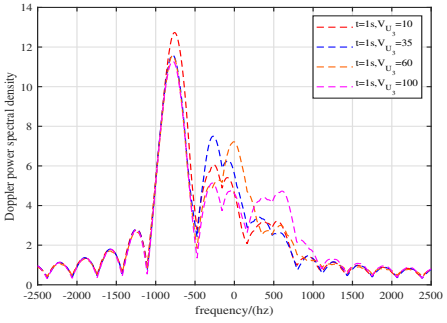

Fig. 15 Temporal Autocorrelation Functions at Different non-communication Node Mobile Velocities

It is evident from the figure that variations in velocity lead to changes in the DPSD, indicating the significant impact of transmitting node mobile velocity on DPSD. In Figure 15, the focus is on the effect of non-communication node mobile velocities on DPSD. It can be observed that the increasing velocity of non-communication nodes results in varying maximum Doppler shifts, causing fluctuations in the DPSD curve.

Figures 13-15 investigate the influence of channelrelated parameters on Doppler Power Spectral Density. The trends observed in Figures 13 and 14 are consistent with conclusions drawn from existing models [21]. The DPSD varies at different time instances, and the curve becomes sharpest when the Doppler frequency matches the maximum Doppler shift. As the transmitting node's mobile velocity increases, the peaks of the DPSD curve continuously shift, and the magnitude of this shift becomes larger with higher transmitting node velocities. Figure 15 demonstrates that changes in non-communication node mobile velocities lead to alterations in the maximum Doppler shift. The DPSD curve's peak exhibits noticeable changes under different mobile velocities. Therefore, it is evident that mobile velocities significantly impact Doppler Power Spectral Density, contributing to variations in the curve's features and characteristics under different circumstances.

4.5 Comparison with other model

To validate the effectiveness of the proposed model, it is compared with the model proposed in reference [21]. The simulation parameters are the same as those mentioned above, except for the number of UAVs. Here, the number of UAVs, N, is set to 2. From Figure 16, it can be observed that the spatial correlation functions of the proposed model and the model in reference [21] exhibit similar trends, validating the theoretical effectiveness of the proposed model in this paper. In summary, the proposed broadband non-stationary channel model for UAV swarms exhibits similarities in statistical characteristics with existing models. However, particular attention needs to be given to the motion parameters of non-communication nodes, as they significantly influence the statistical properties of the channel model.

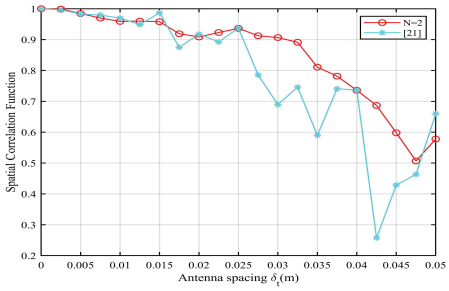

Fig. 16 Comparison of spatial correlation functions under different models.

5. Conclusion

In this paper, we consider the communication scenario of UAV swarms, and a three-dimensional wideband non-stationary channel model for UAV swarm communication is proposed. The model incorporates heterogeneous scattering sources, including line-of-sight (LOS), single-bounce, and double-bounce components. The proposed model introduces time-varying parameters for UAV swarm motion Velocity, inter-UAV distances, departure and arrival angles, while also accounting for the motion states of both transmitting and non-communication nodes. Simulation results demonstrate that the statistical characteristics of the UAV swarm wideband non-stationary channel model are generally consistent with existing models. However, the influence of non-communication nodes on these statistical characteristics cannot be neglected. The proposed wideband non-stationary channel model based on UAVs can provide theoretical support for future research on UAVs-based wideband communication channels.

APPENDIX A
DERIVATIONS OF THE LOS PARAMETERS

The velocity of each node in the UAV swarm is $v_{U_i}, i = 1, 2, nc_j$, and the acceleration is $a_{U_i}, i = 1, 2, nc_j$. The real-time velocity of each node can be represented as:

$$v_{U_i}(t_i) = v_{U_i} + a_{U_i} \times t_i. \tag{19}$$

The movement distance of each node can be represented as:

$$l_{U_i}(t_i) = v_{U_i} \times t_i + \frac{a_{U_i} \times {t_i}^2}{2}, i = 1, 2, nc_j. \tag{20}$$

Therefore, given the initial position of the transmitting node as $\left[P^x_{UAV_1}, P^y_{UAV_1}, P^z_{UAV_1}\right] = \left[0, 0, H_{U_1}\right]$, its time-varying position is represented as :

$$\begin{cases} P^x_{UAV_1} = l_{U_1}(t_i)\cos\phi_{U_1}\cos\gamma_{U_1} \\ P^y_{UAV_1} = l_{U_1}(t_i)\cos\phi_{U_1}\sin\gamma_{U_1} \\ P^z_{UAV_1} = H_{U_1} + l_{U_1}(t_i)\sin\phi_{U_1}\ , \end{cases} \tag{21}$$

where ϕ_{U_1} represents the elevation angle of the transmitting node's movement, and γ_{U_2} represents the azimuth angle of the transmitting node's movement.

Given the initial position of the receiving node as $\left[P^x_{UAV_2}, P^y_{UAV_2}, P^z_{UAV_2}\right] = \left[D_{U_1U_2}, 0, H_{U_2}\right]$, its time-varying position is represented as:

$$\begin{cases} P^x_{UAV_2} = D_{U_1U_2} + l_{U_2}(t_i)\cos\phi_{U_2}\cos\gamma_{U_2} \\ P^y_{UAV_2} = l_{U_2}(t_i)\cos\phi_{U_2}\sin\gamma_{U_2} \\ P^z_{UAV_2} = H_{U_2} + l_{U_2}(t_i)\sin\phi_{U_2}\ , \end{cases} \tag{22}$$

where ϕ_{U_2} represents the elevation angle of the receiving node's movement, and γ_{U_2}represents the azimuth angle of the receiving node's movement.

The initial position of the non-communication node is$\left[P^x_{U_{nc_j}}, P^y_{U_{nc_j}}, P^z_{U_{nc_j}}\right] = \left[D_{U_1U_{nc_j}}, Vd_{U_{nc_j}}, H_{U_{nc_j}}\right]$, and its time-varying position is represented as:

$$\begin{cases} P^x_{U_{nc_j}} = D_{U_1U_{nc_j}} + l_{U_{nc_j}}(t_i)\cos\phi_{U_{nc_j}}\cos\gamma_{U_{nc_j}} \\ P^y_{U_{nc_j}} = Vd_{U_{nc_j}} + l_{U_{nc_j}}(t_i)\cos\phi_{U_{nc_j}}\sin\gamma_{U_{nc_j}} \\ P^z_{U_{nc_j}} = H_{U_{nc_j}} + l_{U_{nc_j}}(t_i)\sin\phi_{U_{nc_j}}\ , \end{cases} \tag{23}$$

where $\phi_{U_{nc_j}}$ represents the elevation angle of the non-communication node's movement, and $\gamma_{U_{nc_j}}$ represents the azimuth angle of the non-communication node's movement.

1.Time-varying channel parameters of the Line-of-Sight (LOS) component

The transmission distance of the LOS component can be calculated using the spatial distance formula:

$$\xi_{pl}(t_i) = \sqrt{\left(T^x_P - R^x_l\right)^2 + \left(T^y_P - R^y_l\right)^2 + \left(T^z_P - R^z_l\right)^2}, \tag{24}$$

where the position of the transmitting antenna T_P is represented by $[T^x_P, T^y_P, T^z_P]$ and the position of the receiving antenna R_l is represented by $[R^x_l, R^y_l, R^z_l]$. The positions of the antennas can be calculated using the following formula.

Let d_T represent the distance from T_P to the center of the transmitting antenna array, and d_R represent the distance from R_l to the center of the receiving antenna array.

$$\begin{cases} d_T = \frac{(N_T+1-2p)\,\delta_T}{2} \\ d_R = \frac{(N_R+1-2l)\,\delta_R}{2} \end{cases}, \tag{25}$$

where δ_T represents the spacing between antennas at the transmitter, δ_R represents the spacing between antennas at the receiver, N_T represents the number of elements in the transmitting antenna array, N_R represents the number of elements in the receiving antenna array, and p and l respectively denote the antenna indices. Therefore, it follows:

$$\begin{cases} T_P^x = l_{U_1}(t_i)\cos\phi_{U_1}\cos\gamma_{U_1} - d_T\cos\theta_T \\ T_P^y = l_{U_1}(t_i)\cos\phi_{U_1}\sin\gamma_{U_1} - d_T\sin\theta_T \\ T_P^z = H_{U_1} + l_{U_1}(t_i)\sin\phi_{U_1} \\ R_l^x = D_{U_1U_2} + l_{U_2}(t_i)\cos\phi_{U_2}\cos\gamma_{U_2} - d_R\cos\theta_R \\ R_l^y = l_{U_2}(t_i)\cos\phi_{U_2}\sin\gamma_{U_2} - d_R\sin\theta_R \\ R_l^z = H_{U_2} + l_{U_2}(t_i)\sin\phi_{U_2}\ , \end{cases} \tag{26}$$

where θ_T and θ_R respectively denote the antenna orientations of the transmitting and receiving antennas. The time-varying Doppler frequency shift of the LOS component is:

$$\begin{aligned} f_{Los}(t_i) &= f_{U_1}(t_i)\left(\cos\phi_{U_1}\cos\gamma_{U_1}\cos\beta_{U_1U_2}(t_i)\right. \\ &+ \left.\sin\phi_{U_1}\sin\beta_{U_1U_2}(t_i)\right) \\ &+ f_{U_2}(t_i)\left(\cos\phi_{U_2}\cos\gamma_{U_2}\cos\beta_{U_1U_2}(t_i)\right. \\ &+ \left.\sin\phi_{U_2}\sin\beta_{U_1U_2}(t_i)\right)\ , \end{aligned} \tag{27}$$

where the maximum Doppler frequency shift of the UAVs is denoted by $f_{U_i}(t_i)\,(i = 1, 2, nc_j)$;$f_{U_i}(t_i) = \frac{v_{U_i}(t_i)}{\lambda}(i = 1, 2, nc_j)$, $v_{U_i}(t_i)$ represents the flight speed of each UAV, λ represents the carrier wavelength, $\beta_{U_IU_2}(t_i)$ represents the elevation angle of the transmitting and receiving nodes, $\beta_{U_IU_2}(t_i) = \arctan\left(\frac{T_P^z - R_l^z}{\sqrt{\left(P_{UAV_2}^x - P_{UAV_1}^x\right)^2 + \left(P_{UAV_2}^y - P_{UAV_1}^y\right)^2}}\right)$.

The time-varying propagation delay of the LOS component is:

$$\tau_{Los}(t_i) = \frac{\xi_{pl}(t_i)}{c}, \tag{28}$$

where c represents the velocity of light.

APPENDIX B
DERIVATIONS OF THE SB PARAMETERS

1. Time-varying channel parameters of the SB_1 component

The transmission distance of the SB_1 component can be calculated using the spatial distance formula:

$$\xi_{SB_1}(t_i) = \xi_{p,S^{n_1}}(t_i) + \xi_{S^{n_1},l}(t_i), \tag{29}$$

$$\xi_{p,S^{n_1}}(t_i) = \sqrt{\left(P_{S^{n_1}}^x - T_P^x\right)^2 + \left(P_{S^{n_1}}^y - T_P^y\right)^2 + \left(P_{S^{n_1}}^z - T_P^z\right)^2}, \tag{30}$$

$$\xi_{S^{n_1},l}(t_i) = \sqrt{\left(R_l^x - P_{S^{n_1}}^x\right)^2 + \left(R_l^y - P_{S^{n_1}}^y\right)^2 + \left(R_l^z - P_{S^{n_1}}^z\right)^2}, \tag{31}$$

where the coordinates of the scatterer S^{n_1} are represented by $[P_{S^{n_1}}^x, P_{S^{n_1}}^y, P_{S^{n_1}}^z]$:

$$\begin{cases} P_{S^{n_1}}^x = R_1\cos\beta_T^{S^{n_1}}\cos\alpha_T^{S^{n_1}} \\ P_{S^{n_1}}^y = R_1\cos\beta_T^{S^{n_1}}\sin\alpha_T^{S^{n_1}} \\ P_{S^{n_1}}^z = H_{U_1} + R_1\sin\beta_T^{S^{n_1}}\ , \end{cases} \tag{32}$$

where R_1 represents the distribution radius of the scatterers near the transmitting node; $\alpha_T^{S^{n_1}}$ and $\beta_T^{S^{n_1}}$ denote the azimuth angle and elevation angle from the transmitting node to scatterer S^{n_1}, respectively, following the VMF distribution and cosine distribution.

The time-varying Doppler frequency shift of the SB_1 component is:

$$\begin{aligned} f_{SB_1} &= f_{U_1}(t_i)\left(\cos\phi_{U_1}\cos\left(\alpha_T^{S^{n_1}}(t_i) - \gamma_{U_1}\right)\cos\beta_T^{S^{n_1}}(t_i)\right. \\ &+ \left.\sin\phi_{U_1}\sin\beta_T^{S^{n_1}}(t_i)\right) \\ &+ f_{U_2}(t_i)\left(\cos\phi_{U_2}\cos\left(\alpha_R^{S^{n_1}}(t_i) - \gamma_{U_2}\right)\cos\beta_R^{S^{n_1}}(t_i)\right. \\ &+ \left.\sin\phi_{U_2}\sin\beta_R^{S^{n_1}}(t_i)\right), \end{aligned} \tag{33}$$

where $\alpha_R^{S^{n_1}}(t_i)$ and $\beta_R^{S^{n_1}}(t_i)$ represent the time-varying azimuth angle and elevation angle from the scatterer S^{n_1} to the receiving node. As shown in Equation 34.

The time-varying propagation delay of the SB_1 component is:

$$\tau_{SB_1}(t_i) = \frac{\xi_{SB_1}(t_i)}{c}. \tag{35}$$

2.Time-varying channel parameters of the SB_2 component

The transmission distance of the SB_2 component can be calculated using the spatial distance formula:

$$\xi_{SB_2}(t_i) = \xi_{p,S^{n_2}}(t_i) + \xi_{S^{n_2},l}(t_i), \tag{36}$$

$$\xi_{p,S^{n_2}}(t_i) = \sqrt{\left(P_{S^{n_2}}^x - T_P^x\right)^2 + \left(P_{S^{n_2}}^y - T_P^y\right)^2 + \left(P_{S^{n_2}}^z - T_P^z\right)^2},$$

$$\begin{cases} \alpha_T^{S^{n_1}}(t_i) = \arccos\left(\frac{\left(P_{S^{n_1}}^x - P_{UAV_1}^x\right)^2 + \left(P_{S^{n_1}}^y - P_{UAV_1}^y\right)^2 + \left(P_{UAV_2}^x - P_{UAV_1}^x\right)^2 + \left(P_{UAV_2}^y - P_{UAV_1}^y\right)^2 - \left(\left(P_{UAV_2}^x - P_{S^{n_1}}^x\right)^2 + \left(P_{UAV_2}^y - P_{S^{n_1}}^y\right)^2\right)}{2\times\sqrt{\left(\left(P_{S^{n_1}}^x - P_{UAV_1}^x\right)^2 + \left(P_{S^{n_1}}^y - P_{UAV_1}^y\right)^2\right)\times\left(\left(P_{UAV_2}^x - P_{UAV_1}^x\right)^2 + \left(P_{UAV_2}^y - P_{UAV_1}^y\right)^2\right)}}\right) \\ \beta_T^{S^{n_1}}(t_i) = \arctan\left(\frac{P_{S^{n_1}}^z - P_{UAV_1}^z}{\sqrt{\left(P_{S^{n_1}}^x - P_{UAV_1}^x\right)^2 + \left(P_{S^{n_1}}^y - P_{UAV_1}^y\right)^2}}\right) \\ \alpha_R^{S^{n_1}}(t_i) = \arcsin\left(\frac{\sqrt{\left(P_{S^{n_1}}^x - P_{UAV_1}^x\right)^2 + \left(P_{S^{n_1}}^y - P_{UAV_1}^y\right)^2}}{\sqrt{\left(P_{UAV_2}^x - P_{S^{n_1}}^x\right)^2 + \left(P_{UAV_2}^y - P_{S^{n_1}}^y\right)^2}}\sin\alpha_T^{S^{n_1}}(t_i)\right) \\ \beta_R^{S^{n_1}}(t_i) = \arctan\left(\frac{P_{S^{n_1}}^z - P_{UAV_2}^z}{\sqrt{\left(P_{UAV_2}^x - P_{S^{n_1}}^x\right)^2 + \left(P_{UAV_2}^y - P_{S^{n_1}}^y\right)^2}}\right), \end{cases} \tag{34}$$

$$\xi_{S^{n_2},l}(t_i)=\sqrt{\left(R_l^x-P_{S^{n_2}}^x\right)^2+\left(R_l^y-P_{S^{n_2}}^y\right)^2+\left(R_l^z-P_{S^{n_2}}^z\right)^2}, \tag{37}$$

(38)

where the coordinates of the scatterer S^{n_2} are represented by $[P_{S^{n_2}}^x, P_{S^{n_2}}^y, P_{S^{n_2}}^z]$:

$$\begin{cases} P_{S^{n_2}}^x = D_{U_1,U_2} - R_2\cos\beta_R^{S^{n_2}}\cos\left(\pi-\alpha_R^{S^{n_2}}\right) \\ P_{S^{n_2}}^y = R_2\cos\beta_R^{S^{n_2}}\sin\left(\pi-\alpha_R^{S^{n_2}}\right) \\ P_{S^{n_2}}^z = H_{U_2} + R_2\sin\beta_R^{S^{n_2}}, \end{cases} \tag{39}$$

where R_2 represents the distribution radius of the scatterers near the receiving node; $\alpha_R^{S^{n_2}}$ and $\beta_R^{S^{n_2}}$ denote the azimuth angle and elevation angle from the receiving node to scatterer S^{n_2}, respectively, following the VMF distribution and cosine distribution.

The time-varying Doppler frequency shift of the SB_2 component is:

$$\begin{aligned} f_{SB_2} &= f_{U_1}(t_i)\left(\cos\phi_{U_1}\cos\left(\alpha_T^{S^{n_2}}(t_i)-\gamma_{U_1}\right)\cos\beta_T^{S^{n_2}}(t_i)\right. \\ &\quad \left.+\sin\phi_{U_1}\sin\beta_T^{S^{n_2}}(t_i)\right) \\ &\quad + f_{U_2}(t_i)\left(\cos\phi_{U_2}\cos\left(\alpha_R^{S^{n_2}}(t_i)-\gamma_{U_2}\right)\cos\beta_R^{S^{n_2}}(t_i)\right. \\ &\quad \left.+\sin\phi_{U_2}\sin\beta_R^{S^{n_2}}(t_i)\right), \end{aligned} \tag{40}$$

where $\alpha_T^{S^{n_2}}(t_i)$ and $\beta_T^{S^{n_2}}(t_i)$ represent the time-varying azimuth angle and elevation angle from the transmitting node to the scatterer S^{n_2}. As shown in Equation 41.

The time-varying propagation delay of the SB_2 component is:

$$\tau_{SB_2}(t_i)=\frac{\xi_{SB_2}(t_i)}{c}. \tag{42}$$

3.Time-varying channel parameters of the SB_3 component

The transmission distance of the SB_3 component can be calculated using the spatial distance formula:

$$\xi_{SB_3}(t_i)=\xi_{p,S^{n_3}}(t_i)+\xi_{S^{n_3},l}(t_i), \tag{43}$$

$$\xi_{p,S^{n_3}}(t_i)=\sqrt{\left(P_{S^{n_3}}^x-T_P^x\right)^2+\left(P_{S^{n_3}}^y-T_P^y\right)^2+\left(P_{S^{n_3}}^z-T_P^z\right)^2}, \tag{44}$$

$$\xi_{S^{n_3},l}(t_i)=\sqrt{\left(R_l^x-P_{S^{n_3}}^x\right)^2+\left(R_l^y-P_{S^{n_3}}^y\right)^2+\left(R_l^z-P_{S^{n_3}}^z\right)^2}, \tag{45}$$

where the coordinates of the scatterer S^{n_3} are represented by $[P_{S^{n_3}}^x, P_{S^{n_3}}^y, P_{S^{n_3}}^z]$:

$$\begin{cases} P_{S^{n_3}}^x = R_3\cos\alpha_T^{S^{n_3}} \\ P_{S^{n_3}}^y = R_3\sin\alpha_T^{S^{n_3}} \\ P_{S^{n_3}}^z = H_{U_1} - R_3\tan\beta_T^{S^{n_3}}, \end{cases} \tag{46}$$

where R_3 represents the radius of the cylindrical distribution of distant scatterers; $\alpha_T^{S^{n_3}}$ and $\beta_T^{S^{n_3}}$ denote the azimuth angle and elevation angle from the transmitting node to scatterer S^{n_3}, respectively, following the VMF distribution and cosine distribution.

The time-varying Doppler frequency shift of the SB_3 component is:

$$\begin{aligned} f_{SB_3}(t_i) &= f_{U_1}(t_i)\left(\cos\phi_{U_1}\cos\left(\alpha_T^{S^{n_3}}(t_i)-\gamma_{U_1}\right)\cos\beta_T^{S^{n_3}}(t_i)\right. \\ &\quad \left.+\sin\phi_{U_1}\sin\beta_T^{S^{n_3}}(t_i)\right) \\ &\quad + f_{U_2}(t_i)\left(\cos\phi_{U_2}\cos\left(\alpha_R^{S^{n_3}}(t_i)-\gamma_{U_2}\right)\cos\beta_R^{S^{n_3}}(t_i)\right. \\ &\quad \left.+\sin\phi_{U_2}\sin\beta_R^{S^{n_3}}(t_i)\right), \end{aligned} \tag{47}$$

where $\alpha_R^{S^{n_3}}(t_i)$ and $\beta_R^{S^{n_3}}(t_i)$ represent the time-varying azimuth angle and elevation angle from the transmitting node to the scatterer S^{n_3}. As shown in Equation 48.

The time-varying propagation delay of the SB_3 component is:

$$\tau_{SB_3}(t_i)=\frac{\xi_{SB_3}(t_i)}{c}. \tag{49}$$

4.Time-varying channel parameters of the SB_{nc_j} component

The transmission distance of the SB_{nc_j} component can be calculated using the spatial distance formula:

$$\xi_{SB_{nc_j}}(t_i)=\xi_{p,Unc_j}(t_i)+\xi_{Unc_j,l}(t_i), \tag{50}$$

$$\xi_{p,Unc_j}(t_i)=\sqrt{\left(P_{Unc_j}^x-T_P^x\right)^2+\left(P_{Unc_j}^y-T_P^y\right)^2+\left(P_{Unc_j}^z-T_P^z\right)^2},$$

$$\begin{cases} \alpha_R^{S^{n_2}}(t_i)=\pi-\arccos\left(\dfrac{\left(P_{S^{n_2}}^x-P_{UAV_2}^x\right)^2+\left(P_{S^{n_2}}^y-P_{UAV_2}^y\right)^2+\left(P_{UAV_2}^x-P_{UAV_1}^x\right)^2+\left(P_{UAV_2}^y-P_{UAV_1}^y\right)^2-\left(\left(P_{UAV_1}^x-P_{S^{n_2}}^x\right)^2+\left(P_{UAV_1}^y-P_{S^{n_2}}^y\right)^2\right)}{2\times\sqrt{\left(\left(P_{S^{n_2}}^x-P_{UAV_2}^x\right)^2+\left(P_{S^{n_2}}^y-P_{UAV_2}^y\right)^2\right)\times\left(\left(P_{UAV_2}^x-P_{UAV_1}^x\right)^2+\left(P_{UAV_2}^y-P_{UAV_1}^y\right)^2\right)}}\right) \\ \beta_R^{S^{n_2}}(t_i)=\arctan\left(\dfrac{P_{S^{n_2}}^z-P_{UAV_2}^z}{\sqrt{\left(P_{S^{n_2}}^x-P_{UAV_2}^x\right)^2+\left(P_{S^{n_2}}^y-P_{UAV_2}^y\right)^2}}\right) \\ \alpha_T^{S^{n_2}}(t_i)=\arcsin\left(\dfrac{\sqrt{\left(P_{S^{n_2}}^x-P_{UAV_2}^x\right)^2+\left(P_{S^{n_2}}^y-P_{UAV_2}^y\right)^2}}{\sqrt{\left(P_{S^{n_2}}^x-P_{UAV_1}^x\right)^2+\left(P_{S^{n_2}}^y-P_{UAV_1}^y\right)^2}}\sin\left(\pi-\alpha_R^{S^{n_2}}(t)\right)\right) \\ \beta_T^{S^{n_2}}(t_i)=\arctan\left(\dfrac{P_{S^{n_2}}^z-P_{UAV_1}^z}{\sqrt{\left(P_{UAV_1}^x-P_{S^{n_2}}^x\right)^2+\left(P_{UAV_1}^y-P_{S^{n_2}}^y\right)^2}}\right), \end{cases} \tag{41}$$

$$\xi_{U_{nc_j},l}(t_i) = \sqrt{\left(R_l^x - P_{U_{nc_j}}^x\right)^2 + \left(R_l^y - P_{U_{nc_j}}^y\right)^2 + \left(R_l^z - P_{U_{nc_j}}^z\right)^2} \tag{51}$$

where the position of the transmitting antenna is $[T_P^x, T_P^y, T_P^z]$, and the position of the non-communication node is $\left[P_{U_{nc_j}}^x, P_{U_{nc_j}}^y, P_{U_{nc_j}}^z\right]$.

The time-varying Doppler frequency shift of the SB_{nc_j} component is:

$$\begin{aligned} f_{SB_{nc_j}}(t_i) &= f_{U_1}(t_i)\left(\cos\phi_{U_1}\cos\left(\alpha_{U_1Unc_j}(t_i) - \gamma_{U_1}\right)\right. \\ &\times\cos\beta_{U_1Unc_j}(t_i) + \sin\phi_{U_1}\sin\beta_{U_1Unc_j}(t_i)\Big) \\ &+ f_{U_2}(t_i)\left(\cos\phi_{U_2}\cos\left(\alpha_{U_2U_{nc_j}}(t_i) - \gamma_{U_2}\right)\right. \\ &\times\cos\beta_{U_2Unc_j}(t_i) + \sin\phi_{U_2}\sin\beta_{U_2U_{nc_j}}(t_i)\Big) \\ &- f_{U_{nc_j}}(t_i)\left[\left(\cos\phi_{U_{nc_j}}\cos\left(\alpha_{U_1Unc_j}(t_i) - \gamma_{Unc_j}\right)\right.\right. \\ &\times\cos\beta_{U_1U_{nc_j}}(t_i) + \sin\phi_{Unc_j}\sin\beta_{U_1U_{nc_j}}(t_i)\Big) \\ &+\left.\left(\cos\phi_{U_{nc_j}}\cos\left(\alpha_{U_2Unc_j}(t_i) - \gamma_{Unc_j}\right)\right)\right] \\ &\times\cos\beta_{U_2U_{nc_j}}(t_i) + \sin\phi_{Unc_j}\sin\beta_{U_2Unc_j}(t_i), \end{aligned} \tag{53}$$

where $\alpha_{U_1U_{nc_j}}, \beta_{U_1U_{nc_j}}$ represents the relative azimuth and elevation angles between the transmitting node and the non-communication node; $\alpha_{U_2U_{nc_j}}, \beta_{U_2U_{nc_j}}$ represents the relative azimuth and elevation angles between the receiving node and the non-communication node, as shown in Equation 54.

The time-varying propagation delay of the SB_{nc_j} component is:

$$\tau_{SB_{nc_j}}(t_i) = \frac{\xi_{SB_{nc_j}}(t_i)}{c}. \tag{55}$$

APPENDIX C
DERIVATIONS OF THE DB PARAMETERS

1.Time-varying channel parameters of the DB_1 component

The transmission distance of the DB_1 component can be calculated using the spatial distance formula:

$$\xi_{DB_1}(t_i) = \xi_{p,S^{n_1}}(t_i) + \xi_{S^{n_1},S^{n_2}} + \xi_{S^{n_2},l}(t_i), \tag{56}$$

$$\xi_{S^{n_1},S^{n_2}} = \sqrt{\left(P_{S^{n_1}}^x - P_{S^{n_2}}^x\right)^2 + \left(P_{S^{n_1}}^y - P_{S^{n_2}}^y\right)^2 + \left(P_{S^{n_1}}^z - P_{S^{n_2}}^z\right)^2}. \tag{57}$$

The time-varying Doppler frequency shift of the DB_1 component is:

$$\begin{cases} \alpha_T^{S^{n_3}}(t_i) = \arccos\left(\dfrac{\left(P_{S^{n_3}}^x - P_{UAV_1}^x\right)^2 + \left(P_{S^{n_3}}^y - P_{UAV_1}^y\right)^2 + \left(P_{UAV_2}^x - P_{UAV_1}^x\right)^2 + \left(P_{UAV_2}^y - P_{UAV_1}^y\right)^2 - \left(\left(P_{UAV_2}^x - P_{S^{n_3}}^x\right)^2 + \left(P_{UAV_2}^y - P_{S^{n_3}}^y\right)^2\right)}{2\times\sqrt{\left(\left(P_{S^{n_3}}^x - P_{UAV_1}^x\right)^2 + \left(P_{S^{n_3}}^y - P_{UAV_1}^y\right)^2\right)\times\left(\left(P_{UAV_2}^x - P_{UAV_1}^x\right)^2 + \left(P_{UAV_2}^y - P_{UAV_1}^y\right)^2\right)}}\right) \\ \beta_T^{S^{n_3}}(t_i) = \arctan\left(\dfrac{P_{S^{n_3}}^z - P_{UAV_1}^z}{\sqrt{\left(P_{S^{n_3}}^x - P_{UAV_1}^x\right)^2 + \left(P_{S^{n_3}}^y - P_{UAV_1}^y\right)^2}}\right) \\ \beta_R^{S^{n_3}}(t_i) = \arctan\left(\dfrac{P_{S^{n_3}}^z - P_{UAV_2}^z}{\sqrt{\left(P_{UAV_2}^x - P_{S^{n_3}}^x\right)^2 + \left(P_{UAV_2}^y - P_{S^{n_3}}^y\right)^2}}\right) \\ \alpha_R^{S^{n_3}}(t_i) = \arcsin\left(\dfrac{\sqrt{\left(P_{S^{n_3}}^x - P_{UAV_1}^x\right)^2 + \left(P_{S^{n_3}}^y - P_{UAV_1}^y\right)^2}}{\sqrt{\left(P_{UAV_2}^x - P_{S^{n_3}}^x\right)^2 + \left(P_{UAV_2}^y - P_{S^{n_3}}^y\right)^2}}\sin\alpha_T^{S^{n_3}}(t)\right), \end{cases} \tag{48}$$

$$\begin{cases} \alpha_{U_1U_{nc_j}}(t_i) = \arccos\left(\dfrac{\left(P_{UAV_{nc_j}}^x - P_{UAV_1}^x\right)^2 + \left(P_{UAV_{nc_j}}^y - P_{UAV_1}^y\right)^2 + \left(P_{UAV_2}^x - P_{UAV_1}^x\right)^2 + \left(P_{UAV_2}^y - P_{UAV_1}^y\right)^2 - \left(\left(P_{UAV_2}^x - P_{UAV_{nc_j}}^x\right)^2 + \left(P_{UAV_2}^y - P_{UAV_{nc_j}}^y\right)^2\right)}{2\times\sqrt{\left(\left(P_{UAV_{nc_j}}^x - P_{UAV_1}^x\right)^2 + \left(P_{UAV_{nc_j}}^y - P_{UAV_1}^y\right)^2\right)\times\left(\left(P_{UAV_2}^x - P_{UAV_1}^x\right)^2 + \left(P_{UAV_2}^y - P_{UAV_1}^y\right)^2\right)}}\right) \\ \beta_{U_1U_{nc_j}}(t_i) = \arctan\left(\dfrac{P_{UAV_1}^z - P_{UAV_{nc_j}}^z}{\sqrt{\left(P_{UAV_{nc_j}}^x - P_{UAV_1}^x\right)^2 + \left(P_{UAV_{nc_j}}^y - P_{UAV_1}^y\right)^2}}\right) \\ \alpha_{U_2U_{nc_j}}(t_i) = \arcsin\left(\dfrac{\sqrt{\left(P_{UAV_{nc_j}}^x - P_{UAV_1}^x\right)^2 + \left(P_{UAV_{nc_j}}^y - P_{UAV_1}^y\right)^2}}{\sqrt{\left(P_{UAV_2}^x - P_{UAV_{nc_j}}^x\right)^2 + \left(P_{UAV_2}^y - P_{UAV_{nc_j}}^y\right)^2}}\sin\alpha_{U_1U_{nc_j}}(t_i)\right) \\ \beta_{U_2U_{nc_j}}(t_i) = \arctan\left(\dfrac{P_{UAV_2}^z - P_{UAV_{nc_j}}^z}{\sqrt{\left(P_{UAV_{nc_j}}^x - P_{UAV_2}^x\right)^2 + \left(P_{UAV_{nc_j}}^y - P_{UAV_2}^y\right)^2}}\right), \end{cases} \tag{54}$$

$$f_{DB_1}(t_i) = f_{U_1}(t_i)\left(\cos\phi_{U_1}\cos\left(\alpha_T^{S^{n_1}}(t_i) - \gamma_{U_1}\right)\cos\beta_T^{S^{n_1}}(t_i) + \sin\phi_{U_1}\sin\beta_T^{S^{n_1}}(t_i)\right) + f_{U_2}(t_i)\left(\cos\phi_{U_2}\cos\left(\alpha_R^{S^{n_2}}(t_i) - \gamma_{U_2}\right)\cos\beta_R^{S^{n_2}}(t_i) + \sin\phi_{U_2}\sin\beta_R^{S^{n_2}}(t_i)\right). \tag{58}$$

The time-varying propagation delay of the DB_1 component is:

$$\tau_{DB_1}(t_i) = \frac{\xi_{DB_1}(t_i)}{c}. \tag{59}$$

2.Time-varying channel parameters of the DB_2 component

The transmission distance of the DB_2 component can be calculated using the spatial distance formula:

$$\xi_{DB_2}(t_i) = \xi_{p,S^{n_3}}(t_i) + \xi_{S^{n_3},S^{n_2}} + \xi_{S^{n_2},l}(t_i), \tag{60}$$

$$\xi_{S^{n_3},S^{n_2}} = \sqrt{\left(P_{S^{n_3}}^x - P_{S^{n_2}}^x\right)^2 + \left(P_{S^{n_3}}^y - P_{S^{n_2}}^y\right)^2 + \left(P_{S^{n_3}}^z - P_{S^{n_2}}^z\right)^2}. \tag{61}$$

The time-varying Doppler frequency shift of the DB_2 component is:

$$f_{DB_1}(t_i) = f_{U_1}(t_i)\left(\cos\phi_{U_1}\cos\left(\alpha_T^{S^{n_1}}(t_i) - \gamma_{U_1}\right)\cos\beta_T^{S^{n_1}}(t_i) + \sin\phi_{U_1}\sin\beta_T^{S^{n_1}}(t_i)\right) + f_{U_2}(t_i)\left(\cos\phi_{U_2}\cos\left(\alpha_R^{S^{n_2}}(t_i) - \gamma_{U_2}\right)\cos\beta_R^{S^{n_2}}(t_i) + \sin\phi_{U_2}\sin\beta_R^{S^{n_2}}(t_i)\right). \tag{62}$$

The time-varying propagation delay of the DB_2 component is:

$$\tau_{DB_2}(t_i) = \frac{\xi_{DB_2}(t_i)}{c}. \tag{63}$$

3. Time-varying channel parameters of the DB_{nc_j} component

The transmission distance of the DB_{nc_j} component can be calculated using the spatial distance formula:

$$\xi_{DB_{nc_j}}(t_i) = \xi_{p,U_{nc_j}}(t_i) + \xi_{U_{nc_j},S^{n_2}}(t_i) + \xi_{S^{n_2},l}(t_i), \tag{64}$$

$$\xi_{UAV_{nc_j},S^{n_2}}(t_i) = \sqrt{\left(P_{S^{n_2}}^x - P_{UAV_{nc_j}}^x\right)^2 + \left(P_{S^{n_2}}^y - P_{UAV_{nc_j}}^y\right)^2 + \left(P_{S^{n_2}}^z - P_{UAV_{nc_j}}^z\right)^2}. \tag{65}$$

The time-varying Doppler frequency shift of the DB_{nc_j} component is

$$f_{DB_{nc_j}}(t_i) = f_{U_1}(t_i)\left(\cos\phi_{U_1}\cos\left(\alpha_{U_1Unc_j}(t_i) - \gamma_{U_1}\right)\times\cos\beta_{U_1U_{nc_j}}(t_i) + \sin\phi_{U_1}\sin\beta_{U_1U_{nc_j}}(t_i)\right) - f_{U_{nc_j}}(t_i)\left[\left(\cos\phi_{Unc_j}\cos\left(\alpha_{U_1U_{nc_j}}(t_i) - \gamma_{Unc_j}\right)\times\cos\beta_{U_1U_{nc_j}}(t_i) + \sin\phi_{U_{nc_j}}\sin\beta_{U_1Unc_j}(t_i)\right) + \left(\cos\phi_{U_{nc_j}}\cos\left(\alpha_R^{S^{n_2}}(t_i) - \gamma_{Unc_j}\right)\cos\beta_R^{S^{n_2}}(t_i) + \sin\phi_{U_{nc_j}}\sin\beta_R^{S^{n_2}}(t_i)\right)\right] + f_{U_2}(t_i)\left(\cos\phi_{U_2}\cos\left(\alpha_R^{S^{n_2}}(t_i) - \gamma_{U_2}\right)\cos\beta_R^{S^{n_2}}(t_i) + \sin\phi_{U_2}\sin\beta_R^{S^{n_2}}(t_i)\right). \tag{66}$$

The time-varying propagation delay of the DB_{nc_j} component is:

$$\tau_{DB_{nc_j}}(t_i) = \frac{\xi_{DB_{nc_j}}(t_i)}{c}. \tag{67}$$

References

[1] L. Gupta, R. Jain and G. Vaszkun, "Survey of Important Issues in UAV Communication Networks," IEEE Communications Surveys Tutorials, vol. 18, no. 2, pp. 1123-1152, Secondquarter 2016.

[2] B. Fei, W. Bao, X. Zhu, D. Liu, T. Men and Z. Xiao, "Autonomous Cooperative Search Model for Multi-UAV With Limited Communication Network,"IEEE Internet of Things Journal, vol. 9, no. 19, pp. 19346-19361, Oct., 2022.

[3] Z. R. Bogdanowicz, "Flying Swarm of Drones Over Circulant Digraph," IEEE Transactions on Aerospace and Electronic Systems, vol. 53, no. 6, pp. 2662-2670, Dec. 2017.

[4] Jie, L. I. , L. I. Sai , and A. H. Shaikh . "Joint Channel and Power Assignment for UAV Swarm Communication based on Multi-agent DRL." IEICE Transactions on communications, vol. E105/B, no. 10, pp. 1249-1257, Dec. 2022.

[5] S. Javaid et al., "Communication and Control in Collaborative UAVs: Recent Advances and Future Trends," IEEE Transactions on Intelligent Transportation Systems, vol. 24, no. 6, pp. 5719-5739, June 2023.

[6] K. Meng, X. He, Q. Wu and D. Li, "Multi-UAV Collaborative Sensing and Communication: Joint Task Allocation and Power Optimization," IEEE Transactions on Wireless Communications, vol. 22, no. 6, pp. 4232-4246, June 2023.

[7] H. An et al., "Measurement and Ray-tracing for UAV Air-to-air Channel Modeling," 2022 IEEE 5th International Conference on Electronic Information and Communication Technology (ICEICT), Hefei, China , pp. 415-420,2022.

[8] N. Stofik, D. W. Matolak and A. Sahin, "Measurement and Modeling of Low-Altitude Air-Ground Channels in Two Frequency Bands," 2022 Integrated Communication, Navigation and Surveillance Conference (ICNS), Dulles, VA, USA, pp. 1-10, 2022.

[9] R. Amorim, H. Nguyen, P. Mogensen, I. Z. Kovács, J. Wigard and T. B. Sørensen, "Radio Channel Modeling for UAV Communication Over Cellular Networks," IEEE Wireless Communications Letters, vol. 6, no. 4, pp. 514-517, Aug. 2017.

[10] Q. Zhu, K. Jiang, X. Chen, W. Zhong and Y. Yang, "A novel 3D non-stationary UAV-MIMO channel model and its statistical properties,"

China Communications, vol. 15, no. 12, pp. 147-158, Dec. 2018.
[11] J. Chen, S. Wu, S. Liu, C. Wang and W. Wang, "On the 3-D MIMO channel model based on regular-shaped geometry-based stochastic model," 2015 International Symposium on Antennas and Propagation (ISAP), Hobart, TAS, Australia, pp. 1-4, 2015.
[12] L. Zeng, X. Cheng, C. -X. Wang and X. Yin, "A 3D Geometry-Based Stochastic Channel Model for UAV-MIMO Channels," 2017 IEEE Wireless Communications and Networking Conference (WCNC), San Francisco, CA, USA, pp. 1-5, 2017.
[13] R. Jia, Y. Li, X. Cheng and B. Ai, "3D geometry-based UAV-MIMO channel modeling and simulation," in China Communications, vol. 15, no. 12, pp. 64-74, Dec. 2018.
[14] Y. Zhang, Y. Zhou, Z. Ji, K. Lin and Z. He, "A Three-Dimensional Geometry-based Stochastic Model for Air-to-Air UAV Channels," 2020 IEEE 92nd Vehicular Technology Conference (VTC2020-Fall), Victoria, BC, Canada, pp. 1-5, 2020.
[15] H. Jiang, Z. Zhang, L. Wu and J. Dang, "Three-Dimensional Geometry-Based UAV-MIMO Channel Modeling for A2G Communication Environments," IEEE Communications Letters, vol. 22, no. 7, pp. 1438-1441, July 2018.
[16] Li Y, Cheng X, " Modelling and simulation for UAV-aided vehicular MIMO communication channels," IET Communications, vol. 13, no. 18, pp. 3044-3051, 2019.
[17] Z. Ma, B. Ai, R. He, Z. Zhong and M. Yang, "A Non-Stationary Geometry-Based MIMO Channel Model for Millimeter-Wave UAV Networks," IEEE Journal on Selected Areas in Communications, vol. 39, no. 10, pp. 2960-2974, Oct. 2021.
[18] K. Jin, X. Cheng, X. Ge and X. Yin, "Three dimensional modeling and space-time correlation for UAV channels", Proc. IEEE 85th Veh. Technol. Conf. (VTC Spring), pp. 1-5, Jun. 2017.
[19] D. W. Matolak and R. Sun, "Air–Ground Channel Characterization for Unmanned Aircraft Systems—Part I: Methods, Measurements, and Models for Over-Water Settings," IEEE Transactions on Vehicular Technology, vol. 66, no. 1, pp. 26-44, Jan. 2017.
[20] X. Cheng and Y. Li, "A 3-D Geometry-Based Stochastic Model for UAV-MIMO Wideband Nonstationary Channels," IEEE Internet of Things Journal, vol. 6, no. 2, pp. 1654-1662, April 2019.
[21] Z. Ma, B. Ai, R. He, G. Wang, Y. Niu and Z. Zhong, "A Wideband Non-Stationary Air-to-Air Channel Model for UAV Communications," IEEE Transactions on Vehicular Technology, vol. 69, no. 2, pp. 1214-1226, Feb. 2020.
[22] J. Bian, C. -X. Wang, Y. Liu, J. Tian, J. Qiao and X. Zheng, "3D Non-Stationary Wideband UAV-to-Ground MIMO Channel Models Based on Aeronautic Random Mobility Model," IEEE Transactions on Vehicular Technology, vol. 70, no. 11, pp. 11154-11168, Nov. 2021.
[23] Z. Ma et al., "Impact of UAV Rotation on MIMO Channel Characterization for Air-to-Ground Communication Systems," IEEE Transactions on Vehicular Technology, vol. 69, no. 11, pp. 12418-12431, Nov. 2020.

Yunhang Lin received his B.S. degree in Communication Engineering from China West Normal University, in 2019, and the M.S. degree in Electronics and Communications Engineering from Jiangsu University of Science and Technology, in 2022. He is currently pursuing Ph.D. degree in Nanjing University of Aeronautics and Astronautics.His research interests include modeling and measurement of UAV communication.

Xiaoyu Dang received the Ph.D.degree in electrical engineering from Brigham Young University,Provo, UT, in 2009. He is currently a Full Professor with the College of Electronics and Information Engineering, Nanjing University of Aeronautics and Astronautics, Jiangsu, China. From 2016 to 2017, he was a Visiting Scholar with The University of Tennessee, Knoxville, USA. His technical interests include coding and modulation, diversity techniques, and reliable transmission of signals in deep space environments.

Dan Fei received the B.S. and M.S degree in School of Electronic and Information Engineering from Beijing Jiaotong University in 2012 and 2014, respectively. He is currently a full technician in School of Electronic and Information Engineering, BJTU. His current research Broadband mobile communication and railway dedicated mobile communication, channel measurement and modeling.

Mengyao Sun received her B.S. degree in Electronic Information Engineering from Anhui Normal Universityin2022She is currently pursuing M.S. degree in Nanjing University of Aeronautics and Astronautics.Her research interests is UAV swarm localization.

Chaoyi Wang received her B.S. degree in Electronics Information Engineering from Nanjing University of Aeronautics and Astronautics, in 2022. She is currently pursuing M.S. degree in Nanjing University of Aeronautics and Astronautics. Her research interest is array signal processing of UAV swarm.

Yongkai Liu received his B.S. degree in School of Physics and Electronic Information Engineering from Henan Polytechnic University in 2021. He is currently pursuing M.S. degree in Nanjing University of Aeronautics and Astronautics. His research interests is cognitive radio networks.